BNL–111745–2015

QUARTERLY PROGRESS REPORT FOR THE PERIOD OCTOBER – DECEMBER 2015

PROJECT TITLE
Development of Improved CZT for Gamma-Ray Spectrometers and Imaging Arrays

Dr. R. B. James

Nonproliferation and National Security Department
Radiation Detector and Nonproliferation R&D
Brookhaven National Laboratory

U.S. Department of Energy

USDOE National Nuclear Security Administration (NNSA),
Office of Nonproliferation and Verification Research and Development (NA-22)

Notice: This report has been authored by employees of Brookhaven Science Associates, LLC under Contract No. DE– SC0012704 with the U.S. Department of Energy.

DISCLAIMER

This report was prepared as an account of work sponsored by an agency of the United States Government. Neither the United States Government nor any agency thereof, nor any of their employees, nor any of their contractors, subcontractors, or their employees, makes any warranty, express or implied, or assumes any legal liability or responsibility for the accuracy, completeness, or any third party's use or the results of such use of any information, apparatus, product, or process disclosed, or represents that its use would not infringe privately owned rights. Reference herein to any specific commercial product, process, or service by trade name, trademark, manufacturer, or otherwise, does not necessarily constitute or imply its endorsement, recommendation, or favoring by the United States Government or any agency thereof or its contractors or subcontractors. The views and opinions of authors expressed herein do not necessarily state or reflect those of the United States Government or any agency thereof.

QUARTERLY PROGRESS REPORT FOR THE PERIOD OCTOBER-DECEMBER 2015

PROJECT TITLE: Development of Improved CZT for Gamma-Ray Spectrometers and Imaging Arrays

webPMIS PROJECT NAME: BL13-CZTBaseProg-PD2Jg, LAB/CONTRACTOR: BNL

B&R CODE: NN20001050 DATE: January 5, 2016

PRINCIPAL INVESTIGATOR: Ralph B. James, BNL, (631) 344-8633

HQ PROJECT MANAGER: Dr. David Beach, DNN R&D, (202) 586-0346

PROGRESS (BY TASK) DURING QUARTER: October 1 through December 31, 2015

This project had sufficient carry-forward to support about 2 months of R&D during FY16. Work on this project was completed at the end of November 2015, and the balance is near zero. The final report has been written, and it will be uploaded into webPMIS once BNL's internal review-and-approval process is complete (expected during the first week of January 2016). Any small remaining balance will be transferred to the CZTS detector development project at that time.

FY 2015 Tasks

Task #1: Perform over 100 runs of CZT material and device characterization experiments for samples produced under different growth experiments and conduct data analysis.

Micro-heterogeneity in Semi-insulating Cd(Zn)Te Crystals

We investigated the temperature (T=290-420 K) dependences (TDs) of the Hall coefficient, R_H, and the Hall carrier mobility, μ_n ($=\sigma R_H$), of semi-insulating $Cd_{0.9}Zn_{0.1}Te$:In crystals. The state of the defect-impurity system (DIS) in the samples after fabrication is not an equilibrium one. Furthermore, the samples previously had been kept in the dark at t = 150 ºC to ensure that their electrical parameters had reached stationary values, viz., equilibrium at t < 150 ºC. The temperature dependence of the Hall coefficient R_H for practically all samples can be described by two activation energies (AEs). At the point where there is a change in the AE, there also is a change in the temperature dependency of the carriers' mobility, from "normal" at a high temperature to an exponential dependency at low temperature. The latter is a manifestation of the collective effect of the drift barriers caused by potential fluctuations due to DIS micro-heterogeneities. At the value of the high-temperature activation energy, there is no barrier component of the carrier mobility, and we can use a classical method for calculating the ionization energy and other parameters for the compensated deep donors (ε_D). For different samples the values ε_D^o (at absolute zero) range from 0.50 to 0.78 eV, and the values of the compensation effect of donors $[D^+]/[D]$ are between 0.3 and 0.98. The low-temperature data, which are affected by strong crystal micro-heterogeneity, cannot be used to describe the ionization energy of donors. Therefore, we propose to represent the activation energy of this area (ε_1) as: $\varepsilon_1 = \varepsilon_D - Y\varepsilon_b$, where ε_b is the height of the drift barrier, calculated from the temperature dependence of the carrier mobility, and Y has a value close to unity, i.e., about 0.5 at strong compensation and 2 at low compensation. The values of ε_b for those samples that we studied lie between 0.05 and 0.35 eV. We also estimated the size of the space-charge region associated with micro-heterogeneities and their concentrations.

The Impact of Compensation on the Detection Properties of n-Cd(Zn)Te Crystals

We studied the electrical characteristics of In-doped Cd(Zn)Te crystals with poorly expressed n-type conductivity during their growth, and also In/Cd(Zn)Te/In-based structures with ohmic contacts and Cr/Cd(Zn)Te/In structures with Schottky barriers, as used in many X-ray and γ-ray radiation detectors. The temperature dependence of the resistivity and the Fermi-level energies in this high-resistivity material were analyzed and explained. We identified the ionization energy and the degree of compensation of the impurities responsible for this material's conductivity at states of high indium doping. Research on the temperature dependence of currents of the volt-ampere characteristics in the ohmic regions and space-charge limited current (SCLC) regions revealed the connection between the crystal's energy and the degree of compensation of the deep level responsible for crystals' dark conductivity and detection properties.

Task #2: Processing of customized crystals and device fabrication

Selective Etching Reveals the Migration and Evolution of Dislocations in Annealed $Cd_{1-x}Zn_xTe$

We report our investigation of the influence of annealing on the behavior of dislocations in cadmium zinc telluride (CZT) crystals and compare the results with the migration of inclusions. The effect of thermal treatment on the defect structure of CZT was studied by selective etching. Bissoli and Inoue etchants were used for revealing dislocation loops, inclusions, and other defects as complementary to, and the most effective for (111)- and (110)-oriented CZT surfaces. The results of selective etching were evaluated by IRM and AFM for a series of systematically annealed CZT single crystals. We determined that the migration of inclusions in CZT is affected by the presence of dislocations. The dissolution of precipitates is appropriate for visualizing the dislocations on the crystal's surface. In addition, we found new material effects by tracking inclusions near dislocation-specific locations after post-growth annealing.

Task #3: Simulate the effects of dislocations and sub-grain boundaries on CZT device performance and establish bounds on the degree to which they can be tolerated for thick (> 10 mm) detectors. Model the defects in and around twins and sub-grain boundaries and simulate their effects on carrier transport.

This task is complete. We continue to gather additional data required to more accurately model the effects of dislocations and sub-grain boundaries on CZT device performance.

COMMENTS (BY TASK): See the six publications and seven presentations during this quarter for more details.

Task #1: Perform over 100 runs of CZT device characterization experiments at the NSLS for samples produced under different growth experiments and conduct data analysis.

- **X-ray white beam transmission and topography measurements for imaging dislocations, precipitates, twins, and other lattice imperfections.**
- **X-ray rocking curves for mapping and measuring crystal's mosaicity, perfection, and residual strain.**
- **Broad-area and micron-scale X-ray mapping of carrier transport properties and detector response.**

- **Micron-scale X-ray response mapping for different incident energies to characterize surface and edge effects.**
- **Pockels effect measurements.**
- **Etch pit analysis.**
- **Optically induced DLTS measurements.**
- **High-spatial-resolution photoluminescence mapping around defects.**
- **Secondary ion mass spectrometry of impurities within inclusions and other defects.**
- **X- and gamma-ray spectroscopic measurements.**
- **Data documentation.**
- **Data analysis.**
- **Generate reports and scientific publications.**

Micro-heterogeneity in Semi-insulating Cd(Zn)Te Crystals

Electrical measurements often focus on the temperature dependence (TD) of the resistivity. Such measurements take into account the TD of the carriers' mobility (usually observed on low-resistivity crystals to be μ = 750-1100 $cm^2/V\cdot s$ for electrons in the region 20-150 ^oC). The carrier mobility and resistivity can then be used to identify the TD of the carrier concentration. Electrical measurements of the TD of the mobility are justified, since for semi-insulating samples, optical techniques, such as the TOF method, can be used to gain greater confidence in the measured values. However, in the case of non-equilibrium experiments, the TD of the mobility for non-equilibrium (photo) carriers can differ substantially from that of equilibrium (dark) carriers.

CZT samples in the form of a rectangular parallelepiped with dimensions of $12\times2\times1.5$ mm^3 were fabricated from $Cd_{0.9}Zn_{0.1}Te$:In crystal ingots grown by Bridgman methods -- a) under a high pressure inert atmosphere, wherein the concentration of the indium dopant in the melt was $C_o=4\times10^{17}cm^{-3}$; and, b) in its own atmosphere, in closed containers, where $C_o=5\times10^{17}$ cm^{-3}. We studied a total of 26 semi-insulating samples fabricated from 19 ingots. Current contacts and two pairs of Hall symmetrical contacts were formed by the precipitation of copper from a drop of $CuSO_4$, followed by alloy soldering (In-Sn). Measurements were carried out using direct current in a magnetic field with an induction of 0.5 T. Signals were fixed by the electrometer with an input resistance of 10^{12} Ω and a sensitivity of 0.1mV. We investigated the TD (T = 290-420 K) of the Hall coefficient, R_H, and the Hall mobility, $\mu = \sigma R_H$ (σ is the specific conductivity) of the current carriers.

Directly after fabricating the samples, we measured their resistivity that, except for some of the final ingot sections, lies within (2×10^8-2×10^{10}) $\Omega\cdot cm$ at T=290-295 K. At the same time, the Hall signals at this temperature are not fixed, or are fixed at a level that corresponds to values of $\mu\approx10$ $cm^2/V\cdot s$. In all samples, the electrons are the major carriers of current, according to the sign of the Hall voltage.

Up to 100 °C, the values of R_H and μ are isothermally stable and reproducible, but at t > 100 °C (the dashed lines in the figure) isothermal changes occur. At 150 ^oC, the stationary values of the electrical characteristics (ECs) of various samples were achieved after holdup times from 30 minutes up to several hours. Thus, the multiplicity of the increase in the values, μ_n and R_H, are close enough such that there are small noticeable changes in the resistivity ($\rho = R_H/\mu$) during the process of maintaining the samples'

temperature at 150 ^{o}C. However, at room temperature, these changes are more substantial, and the resistivity of different samples ranges from 10^9 to 3.5×10^{10} Ω-cm. After repeatedly cooling and heating these treated samples, no isothermal EC relaxations were observed. So, we assume that at t <150 ^{o}C, the state of defect-impurity system (DIS) in these samples is at equilibrium. This statement remained valid until the samples were kept in the dark (where they do not undergo any photo-excitation).

The temperature-dependent electrical characteristics of two samples, transferred previously into equilibrium states, were typical for all the samples. It is evident that the dependence, $\lg R_H=f(10^3/T)$, is described by two exponents with different activation energies, of which we denote the low-temperature one as ε_1 and high-temperature one as ε_D. At point P, where a change in the activation energy takes place, there also is a change in the nature of the temperature dependence of carrier mobility from the weak "normal" state at high temperature, to an exponential one with activation energy ε_b at low temperature (hereafter this dependence is called the barrier). In different samples, the value of ε_D lies within (0.50-0.78) eV, and the value of ε_b is within (0.05-0.35) eV. However, generally a high ε_b occurs in samples with a large difference between ε_1 and ε_D.

The situation changes radically when samples maintained for a certain time at 150 ^{o}C undergo photo-excitation at room temperature. For illustration, we chose a selected sample in which the equilibrium state was achieved through a 300-minute conditioning at 150 ^{o}C. It is evident that the photo-excitation leads to a strong decrease in mobility and an increase of ε_b: 1 – 0.48 eV; 2 – 0.18 eV; 3 – 0.09 eV. Thus, the greater the deviation from the equilibrium state, the stronger is the effect of the photo-excitation on the Hall electron mobility in the dark. Such photo-excitation influence on the crystal DIS can be characterized as a photochemical reaction (PCR).

The most likely way to explain the two activation energies of the R_H TD is by the following model: In a semi-insulating n-type crystal, there are two types of deep donors (D_1 and D_2) with different ionization energies (ε_{D1} and ε_{D2}) and compensating acceptors A (several types of the latter do not change the situation). Then, we can solve the electro-neutrality equation, $[D_1^+]+[D_2^+]=[A^-]$. The calculation was undertaken for the temperature interval of 280-440 K, and the ionization energies of donors from the interval if 0.3-0.75 eV were obtained. It was apparent that a) if $\varepsilon_{D2}-\varepsilon_{D1}<5kT$, then the electron-concentration TD is described by one activation energy; and, b) two activation energies are needed to assure that there is a realistically high degree of compensation of the more shallow donors D_1.

Therefore, we propose a model that reveals the existence of micro-heterogeneities in the spatial distribution of deep donors of only one variety, and/or the compensating acceptors. With this approach, micro-sized areas appear in which the EC differs from those in the crystal matrix, so leading to potential fluctuations in relief. Under certain conditions, such fluctuations may be the cause of the carrier's exponential growth in mobility with the crystal's increasing temperature. This should not be seen in micro-sized areas, but only in much wider space-charge regions (SCRs).

Fluctuations in potential relief, manifested through drift barriers, change the activation energy of the carrier-concentration TD. Therefore, we assume that the high-temperature activation energy, ε_D, is the true donor-ionization energy. At the same time, we foresee the relationship between ε_1 and ε_D as $\varepsilon_1 = \varepsilon_D-Y\varepsilon_b$, wherein the coefficient Y takes a value close to 1: From 0.5 with strong donor compensation to 2 for weak compensation. In different samples, the degree of donor compensation, $[D^+]/[D]$, determined from the analysis of the high-temperature areas $R_H(T)$, varies from 0.3 to 0.98.

Where the SCR overlap disappears, the screening length, L_D, should be commensurate with the distance between the fluctuation centers, l_f. Therefore, putting $L_D=0.5\ l_f$, we estimated the average distance between

the fluctuation centers. The screening length was calculated based on the crystal's temperature, T, the concentration of free current carriers, *n*, and the material's dielectric permittivity ε using the formula

$$L_D = \sqrt{\frac{\varepsilon\varepsilon_0 kT}{e^2 n}}.$$

For sample 2 at T = 365 K, n = 2.2×10^9 cm^{-3} and ε≈10, our calculation gives $L_D = 0.9\times10^{-2}$ cm, and $l_f = 1.8\times10^{-2}$ cm. We estimate the concentration of the fluctuation as $N_f=2\times10^5$ cm^{-3}. With these calculated SCR parameters, their influence on the carriers' mobility is essential even in state 2, because they occupy almost half of the crystal's volume. The most important feature in this case may be the mechanism of carrier scattering on isolated SCRs, which together with the mechanism of scattering on lattice vibrations, dominate the poor TD of the mobility.

The Impact of Compensation on the Detection Properties of n-Cd(Zn)Te Crystals

The fewer imperfections in Cd(Zn)Te compared to other compound semiconductor materials and its slightly wider band gap than CdTe allow us to produce low-noise electronic devices with good carrier transport properties. Despite the promise of Cd(Zn)Te containing 5-10% Zn, which was demonstrated in the early 1990s during the development as a material substrate for Hg(Cd)Te epitaxial layers, technological problems with the electrical and transport properties hinder the realization of the full potential for such detectors. Only careful selection at all stages of producing the material and fabricating the detectors ensures the achievement of physical properties that will satisfy the practical requirements for radiation detection. For example, we must resolve the problem of the low yield of satisfactory commercial products and take the appropriate steps needed to reduce the high cost of the devices.

Recently, the most popular method for growing doped CdTe and Cd(Zn)Te crystals for manufacturing detectors and spectrometers has been the vertical zone-melting method via a tellurium solution. The advantage of this method is that we can grow crystals at a lower temperature (750 °C) and additionally assure material cleaning via a tellurium-zone purification process. Such as-grown crystals have found use in manufacturing X- and γ-ray spectrometric detectors.

For the studies discussed in this paper, we grew indium-doped Cd(Zn)Te crystals by modified zone melting from a solution melt in excess tellurium. In a quartz ampoule, we placed monolithic specimens of indium-doped Cd(Zn)Te polycrystals (with an indium concentration of $C_0=5\times10^{17}$ cm^{-3}) and cylindrical tellurium specimens. After creating a vacuum (~ 10^{-3} Torr) in the ampoule, it was placed in our crystal-growth setup at an angle of 45° ± 10° to the vertical. Growth of the crystal was achieved by moving the ampoule containing the material through a zone heater at a speed of 5 mm per day, whilst simultaneously rotating it around an axis at a rate of 5-6 turns per minute.

Here, we discuss the results of our research on the properties of indium-doped Cd(Zn)Te. We determined the nature, depths, arrangements, and the degree of compensation of the deep level that is responsible for the dark currents in crystals with ohmic contacts. We elucidated the connections between these parameters and the detection properties for Cr/Cd(Zn)Te/In structures with Schottky contacts fabricated with these crystals.

Crystals were grown via a tellurium solution-melt at 800 ^oC by zone melting of a polycrystalline specimen in a quartz ampoule, which was moved through a heater zone at a rate of 2 mm per day. The polycrystalline specimens were synthesized at 1150 ^oC. For our research, crystals of the appropriate shape were cut from different parts of the ingot. The crystals differed in their electro-physical properties; accordingly, they were named type 1 or type 2. Measurements of the crystals' band gap were undertaken to determine the

homogeneity of the zinc content in both types of crystals. As is known, the band-gap of Cd(Zn)Te is linearly dependent on the zinc content. We used the linear dependence of the Cd(Zn)Te band-gap on zinc content, *x*, to determine its value

$$E_g = E_{go} + a \times x \quad , \tag{1}$$

where E_g is Cd(Zn)Te's band-gap, E_{go} is the CdTe band-gap, and *a* is the proportionality coefficient. Here, E_{go} at 300 K is 1.496 eV. The Cd(Zn)Te band-gap was determined from the optical absorption spectra, after taking into consideration the effect of multiple reflections.
Research was conducted on the absorption edges to determine the band-gap of the Cd(Zn)Te samples. For optical measurements, the Cd(Zn)Te wafers were ground and polished to a thickness of 40-50 μm.

After these treatments, a layer is formed on the single crystal's surface that can complicate the optical measurements for the width of the band-gap. To remove this defective near-surface layer, we chemically etched the sample in a bromine-methanol solution. By step-by-step etching for 20-second intervals, we removed a surface layer of 20-25-μm thickness.

The determination of the width of the band-gap, E_g, for a direct band-gap semiconductor gives an absorption coefficient

$$\alpha(h\nu) = A(h\nu - E_g)^{1/2} \quad . \tag{2}$$

Therefore, we plotted the absorption curves $\alpha(h\nu)$ in the coordinates of α^2 vs. photon energy, $h\nu$. The absorption coefficient, α, was calculated by the formula:

$$\alpha = \frac{1}{d}\ln\left\{\frac{(1-R)^2}{2T} + \left[\frac{(1-R)^4}{4T^2} + R^2\right]^{1/2}\right\}, \tag{3}$$

which is the solution of the equation for the sample's optical transmission, considering multiple reflections within the sample

$$T = \frac{(1-R)^2 \exp(-\alpha d)}{1 - R^2 \exp(-2\alpha d)}, \tag{4}$$

where *d* is the thickness of the sample, and *R* is the coefficient of reflection for the semiconductor-air interface, adopted in the studied spectral range of interest as 0.25.

Fig. 1 shows the results of our measurements of the absorption coefficient. As shown in Fig. 1, a relatively slow change of α in the crystal's area of transparency is changed to one of steep increases at $h\nu > 1.53$ eV. In the area of $\alpha > 100$ cm^{-1}, one can plot a straight section that cuts the axis of photon energies at a value of 1.543 eV. The band-gap of samples cut from various parts of the crystal differed within the range of 1.540-1.543 eV. Thus, using the known relationship of the band-gap to the zinc content, we can assert that the zinc composition in Cd(Zn)Te crystals of type 1 and type 2 is almost identical.

To study the crystals' electro-physical properties, we attached ohmic contacts to crystals cut from different parts of the ingot. The size of the crystals was 5x5 mm^2. Their thickness was 0.8-2.0 mm. After mechanical treatment, the crystal's surface was etched in a bromine-methanol solution and then washed in methanol. Before depositing metal on the crystal's surface, it was treated for 10-15 minutes in an argon plasma at a voltage of 300-350 V at a current of 35-50 mA. Ohmic contacts were formed for the n-type semi-insulating Cd(Zn)Te crystals by the thermal evaporation of indium in a vacuum. A contact of 4x4 mm^2 was formed by molybdenum masks. Further investigation of the In/Cd(Zn)Te/In structures was undertaken.

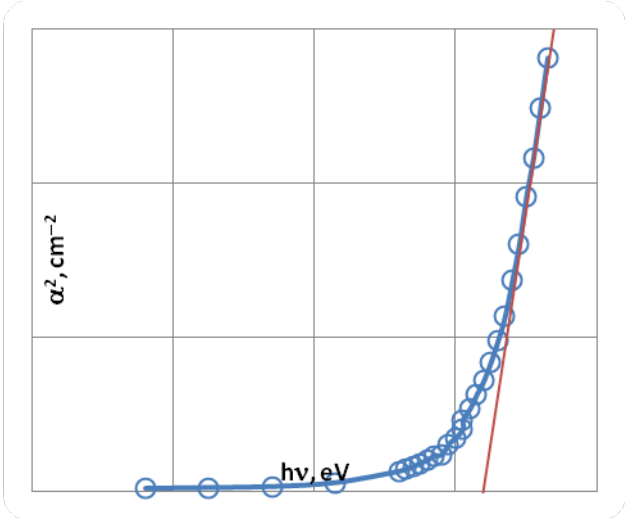

Fig. 1. The dependence of the absorption coefficient of n-Cd(Zn)Te crystals of 20-25 μm- thickness at a temperature of 300 K.

The measurements of the characteristics of the dark current-voltage (*I-V*) were carried out at different temperatures. Fig. 2 shows the I-V characteristics of In/Cd(Zn)Te/In structures for crystals of type 1.

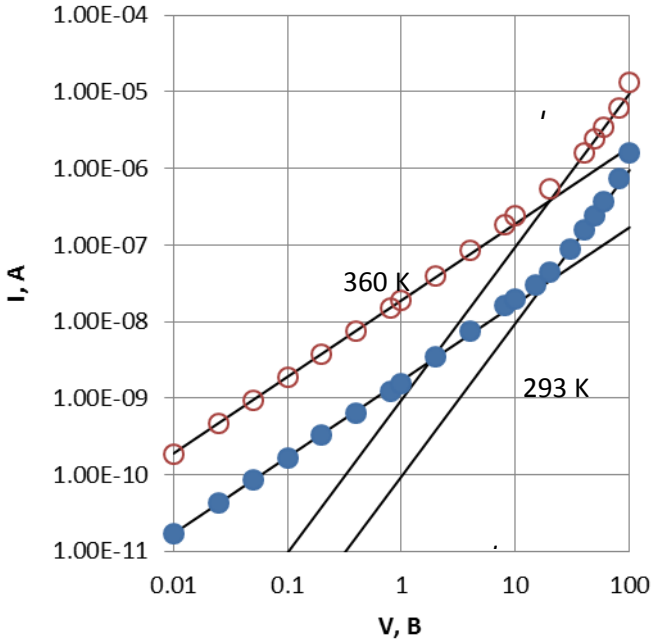

Fig. 2. In/Cd(Zn)Te/In (*I-V*) structures at 293 K (filled circles) and at a temperature of 360 K (open circles). The solid lines show the $I \sim V$ and $I \sim V^2$ areas. The crystal is of type 1. Similar (*I-V*) characteristics for a crystal of type 2 are shown in Fig. 3.

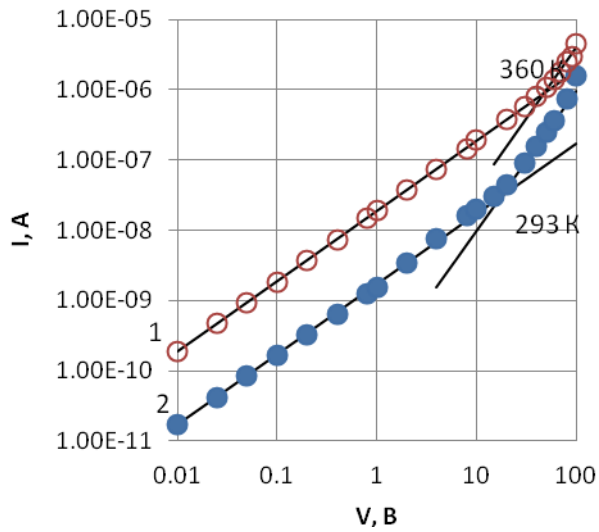

Fig. 3. *I-V* structures with ohmic In/Cd(Zn)Te/In contacts at 293 K (filled circles), and at a temperature of 360 K (open circles). The solid lines show the $I{\sim}V$ and $I{\sim}V^2$ areas for a type-2 crystal.

The *I-V* characteristics of type-1 and type-2 samples displayed certain similarities, but there were significant differences. One common element in the *I-V* characteristics behavior of type-1 and type-2 crystals is that the ohmic area $I{\sim}V$ undergoes a change to a quadratic dependence on the voltage $I{\sim}V^2$ at voltage V_o. The voltage, V_o, is determined by an intersection point of the $I{\sim}V$ and $I{\sim}V^2$ lines after extrapolation. Such *I-V* behavior is explained by the model of space-charge-limited currents (SCLCs). An important *I-V* characteristic is the temperature-dependence of the voltage V_o. Moreover, for type-1 crystals this dependence is weak compared for type-2 crystals (i.e., V_o vs. temperature is quite strong for type 1). Importantly, we note that the resistivity of the crystals, as determined from their linear (*I-V*) plots, was close for both sets of crystals. The resistivity for crystals of type 1 was ~2×10^9 Ω·cm, and for crystals of type 2, the resistivity was ~ 10^9 Ω·cm; both values are obtained at a temperature of 293 K.

The dependence of the resistivity ρ(T) on the temperature of the Cd(Zn)Te crystals from different parts of the ingot was studied separately The results are shown in Fig. 5. The conductivity activation energies, *ΔEs*, of crystals taken from different parts of the ingot were determined from the temperature dependence of the resistivity. A value of 0.78-0.81 eV was obtained for type-1 crystals and 0.55-0.6 eV for type-2 crystals.

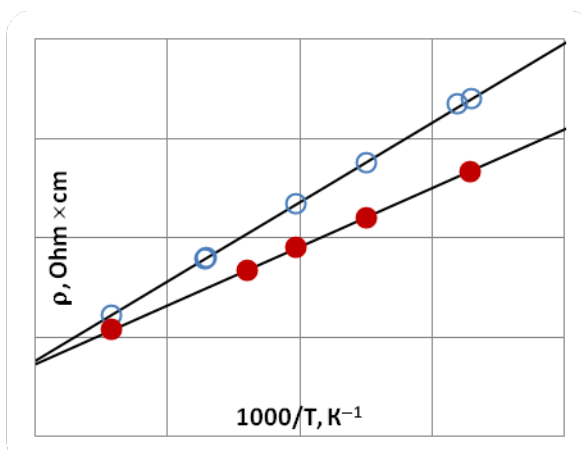

Fig. 5. The temperature dependence of the resistivity for crystals from different parts of the ingot: Open circles - type 1; filled circles - type 2.

The n-type Cd(Zn)Te crystals we studied definitely are compensated semiconductors that have uncontrolled concentrations of impurities and defects, whose concentrations could be substantial. The temperature dependence of the resistivity of Cd(Zn)Te crystal is described by an exponential dependence with an activation energy, ΔE. Analyzing the dark dependence of the Cd(Zn)Te resistivity versus temperature, we obtain important information about the temperature dependence of the position of the Fermi level in the band-gap, plus information about nature of the impurities that determine the conductivity. To estimate the compensation degree of the energy level that determines the dark conductivity, we assume that the position of the Fermi level and the material's conductivity are determined by a donor with energy, E_d, and concentration, N_d, and the concentration of compensating acceptors is N_a. For a semiconductor with such impurities, the electro-neutrality equation takes the following form:

$$p + N^+_d = n + N^-_a \,, \qquad (6)$$

where n and p are the concentrations, respectively, of electrons and holes in the conduction and valence bands, and N^+_d. and N^-_a are the concentrations of ionized donors and acceptors, respectively.

Then, the electro-neutrality equation can be written as

$$p + \frac{N_d}{1+\exp\left(\frac{\Delta\mu - E_d}{kT}\right)} = n + \frac{N_a}{1+\exp\left(\frac{E_a - \Delta\mu}{kT}\right)}, \qquad (7)$$

where

$$n = \frac{N_c}{1+\exp\left(\frac{E_g - \Delta\mu}{kT}\right)} \qquad (8)$$

$$p = N_v \frac{N_v}{1+\exp\left(\frac{\Delta\mu}{kT}\right)}. \qquad (9)$$

$\Delta\mu$, E_d and E_a are the depth of the Fermi, donor, and acceptor levels, respectively, which are counted from the edge of the valence band; the density of states in relevant bands is given by $N_c = 2(m_n k/2\pi\hbar)^{3/2}$ and $N_v = 2(m_p k/2\pi\hbar)^{3/2}$; the effective masses m_n and m_p of electrons and holes in Cd(Zn)Te are taken as $0.11m_o$ and $0.63m_o$, respectively, where m_o is the electron mass in a vacuum. The temperature dependence of the band-gap $E_g(T)$ can be represented as:

$$E_g(T) = E_{go} - \gamma \cdot T, \qquad (10)$$

where E_{go} = 1.68 eV, and the temperature coefficient $\gamma = 4.0\times10^{-4}$ eV·K^{-1}. The $\Delta\mu$ can be determined from the expression for the resistivity

$$\rho = \frac{1}{q(n\mu_n + p\mu_p)} \qquad (11)$$

$$\Delta\mu = E_g + kT\ln\left(\frac{1 \pm \sqrt{1 - 4q^2\rho^2\mu_n\mu_p N_v N_c \exp\left(-\frac{E_g}{kT}\right)}}{2q\rho\mu_n N_c}\right), \qquad (12)$$

where the sign ± designates + for the n-type semiconductor and – for the p-type semiconductor. We note that the energy, $\Delta\mu$, is counted from the edge of the valence band. The values μ_n and μ_p of the electron and hole mobility at 293 K are adopted as equal to 700 and 70 $cm^2/(V\cdot s)$, respectively. The expressions for the temperature dependencies of mobility are given by Eq. (13) according to:

$$\mu_n = 4.0\times10^6 T^{-3/2}\ cm^2/(V\cdot s), \tag{13}$$

$$\mu_p = 4\times10^5 T^{-3/2}\ cm^2/(V\cdot s). \tag{14}$$

Fig. 6 shows the curves obtained by the above equations. In equation (11), the experimental temperature dependence of resistivity is substituted. Equation (7) is solved numerically relative to $\Delta\mu$. The concentrations and depth of the donor and acceptor levels (or N_a/N_d) are selected by fitting the experimental and calculated curves for $\Delta\mu(T)$.

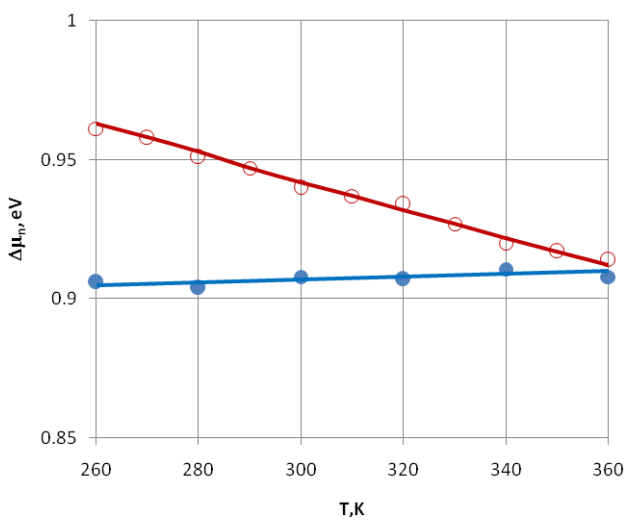

Fig. 6. Temperature dependence of the Fermi level position: Filled circles are for crystals of type 1, open circles are for crystals of type 2. The solid lines show the calculated results.

We note that the temperature dependence $\Delta\mu(T)$ found from the experimental temperature dependence $\rho(T)$ can be obtained only at a single combination of E_d and N_a/N_d. Coincidence between the calculations and the experiment findings is obtained at E_d ~ 1.0 eV and N_a/N_d = 0.93-0.96 for a crystal of type 2 and E_d ~ 0.8-0.82 eV and N_a/N_d =0.03-0.05 for a crystal of type 1. Thus, the deep-donor level determines the dark conductivity of the crystals' inside and at the end of the ingot. Otherwise, the crystal is poorly compensated. Our conclusions confirm our analysis of the SCLC's temperature dependence. According to other data, if the voltage V_o is independent or weakly dependent on temperature, then the crystal is poorly compensated; for highly compensated samples, V_o greatly depends on temperature. According to the research results shown in Figs. 2 and 3, we can clearly conclude that the crystals of type 1 are slightly compensated, and crystals of type 2 are strongly compensated.

Thus, crystals of type 1 and type 2 have similar resistivity (~ 2×10^9 Ω·cm and ~ 10^9 Ω·cm), but differ strongly by their degrees of compensation. In terms of the production of detectors for ionizing radiation, crystals of both type 1 and type 2 have good electro-physical parameters. Since these crystals differ significantly by their degree of compensation, we consider it appropriate and important to examine the relationship between this parameter and the detection properties of structures fabricated from these crystals. To study the detection properties, a structure with ohmic contacts formed by an In/Cd(Zn)Te/In structure proved unsuitable, because the *I-V* area with a relatively weak current dependence on voltage is limited by

the SCLC. The typical voltage value, V_o, for crystals of thickness ~ 1 mm at 293 K is ~ 15-25 V. The electric field strength, which corresponds to this voltage, E~10^2 V/cm, is insufficient for the effective operation of the detector. Using a rectifying contact instead of an ohmic one allowed us to substantially "extend" the *I-V* characteristic section with weak current dependence on the voltage. Chromium was used as the metal to fabricate contacts of such type. The indium ohmic contacts were removed by polishing. After chemical treatment in a solution of bromine in methanol, one crystal surface was covered by chromium through thermal deposition in a vacuum, and the opposite side was coated by indium. Before metal deposition, the surface was treated differently in an argon plasma under conditions of 300-350 V and current of 35-50 mA before depositing indium and at 500-550 V and a current of 15-20 mA before depositing chromium. The contacts were 4x4 mm^2. Thus, Cr/Cd(Zn)Te/In structures were created. The *I-V* characteristics of these structures are shown in Fig. 7.

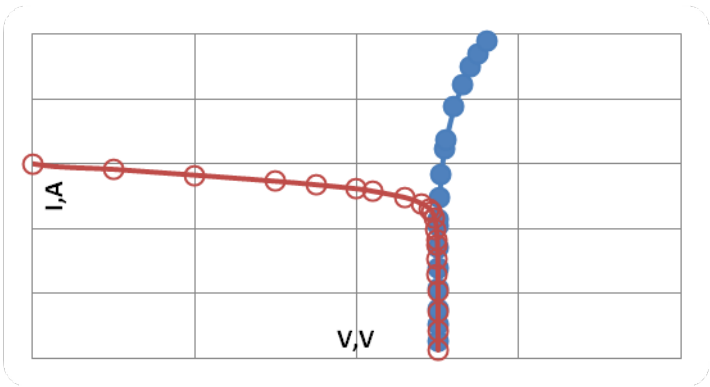

Fig. 7. *I-V* characteristics of the Cr/Cd(Zn)Te/In detector at 293 K: Filled circles – 'plus' on the chromium contact. Empty circles – 'minus' on the chromium contact.

As shown in Fig. 7, the current's weak rise on voltage for the Cr/Cd(Zn)Te/In structure is substantially different than that for an In/Cd(Zn)Te/In with the same sized crystal and the same contact area. Thus, the lower leakage current for the Cr/Cd(Zn)Te/In structure assures a significantly greater strength of the electric field in a crystal with a thickness of ~ 1 mm than does the In/Cd(Zn)Te/In structure. Using the *I-V* characteristics of such structures, we can determine the differential resistance, *dI/dV*, versus voltage *V* (Fig. 8).

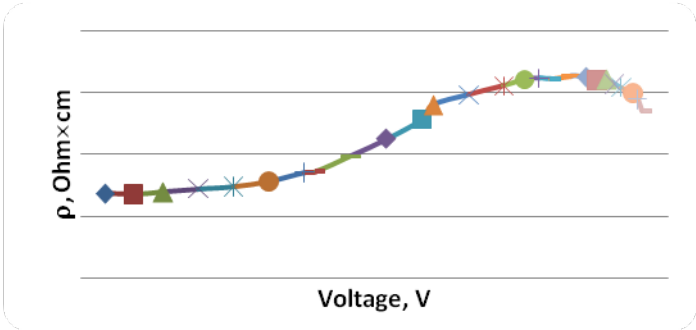

Fig. 8. The differential dependence of the resistance on the Cr/Cd(Zn)Te/In structure of the voltage ('minus' bias to the chromium contact) at 293 K.

As shown in Fig. 8, the structure's differential resistance at a voltage of ~100 V is equal to ~ 2×1011 Ω·cm, which is significantly greater than the crystal's resistivity (~2×109 Ω·cm at 293 K). Thus, the formation of the rectifying contact led to a significant increase of the Cr/Cd(Zn)Te/In structure's tension with a moderate increase in dark current, which did not exceed 1 nA at a voltage of 300-400 V at ~ 293 K. We note that Cr/Cd(Zn)Te/In structures, which were fabricated from crystals of type 1 and type 2, had similar *I-V* characteristics (Fig. 7 and Fig. 8 show typical *I-V* characteristics).

An important parameter that seriously affects the detector efficiency is the mobility-lifetime product for electrons, $\mu_e \tau_e$. The mobility-lifetime product, $\mu_e \tau_e$, can be estimated by measuring the photo-response with gamma irradiation (i.e., gamma spectroscopy) as a function of the strength of the electric field (or the applied bias voltage) at room temperature. Then, the electron mobility-lifetime product, $\mu_e \tau_e$, can be obtained from the Hecht equation. For an approximation of only one type of charge carrier, the Hecht equation takes the form:

$$CCE \approx \frac{\mu_e \tau_e E}{d}\left[1 - \exp\left(\frac{-d}{\mu_e \tau_e E}\right)\right] \qquad (15)$$

Here, $\mu_e \tau_e$ is the mobility-lifetime product, and E is the strength of the electric field. To determine this important parameter, we measured the dependence of the energy spectra on the applied voltage for irradiation by an uncollimated 59.5-keV ^{241}Am gamma-ray source.

The positions of the photopeaks (channels) taken from the gamma-ray spectra are proportional to the charge-collection efficiency (CCE). The value of $\mu_e \tau_e$ can be determined by plotting the dependence of the photopeaks' positions on the applied voltage (see Fig. 9).

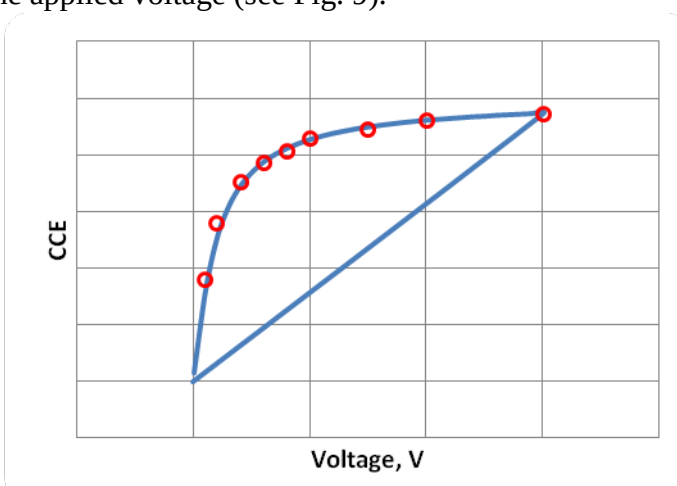

Fig. 9. Photoresponse dependence on the applied voltage for irradiation by an uncollimated 59.5-keV ^{241}Am gamma source from the chromium contact side for the Cr/Cd(Zn)Te/In structure. The unfilled circles show data for the power source 'minus' connected to the chromium contact side. The solid line is the simulated CCE curve for $\mu_e \tau_e = 1.5\times10^{-3}$ cm^2/V. The temperature was 293 K.

Using such techniques the product $\mu_e \tau_e$ was determined to be 1.5×10^{-3} cm^2/V for crystals of type 1, and $\mu_e \tau_e = 5.0\times10^{-4}$ cm^2/V for crystals of type 2. For example, Fig. 9 shows the measurements for crystals of type 1.

Thus, from our research we found that the product $\mu_e \tau_e$ for poorly compensated crystals of type 1 was about three times larger than the product $\mu_e \tau_e$ for highly compensated crystals of type 2.

The conclusions obtained by analyzing the CCE measurements are confirmed by the gamma-ray spectral measurements for samples with Cr/Cd(Zn)Te/In planar structures for irradiation by an uncollimated 59.5-keV ^{241}Am source. Fig. 10 shows the Cr/Cd(Zn)Te/In structure gamma-spectra fabricated on crystals of type 1 and type 2.

Fig. 10 shows that for a crystal taken from the end of the ingot, there is a greater peak-to-valley ratio, indicating better charge collection in these structures, as well as a narrower peak corresponding to the

energy of 59.5 keV. For the best samples from the ingot, we obtained a FWHM of 4.2-4.5 keV. It is important to note that the detector fabricated with the crystals of type 1 has registered cesium-137 isotope radiation at 662 keV, while detectors based on crystals of type 2 did not register a 662-keV photopeak. From our point of view, this can be due to the fact that the space charge region (SCR) at the same voltage in the detectors of type 2 is significantly smaller than in the detectors of type 1. The SCR should be as wide as possible so that more of the photons incident on the detector will be absorbed in that region.

In conclusion, based on studies of the temperature dependence of the *I-V* data in the ohmic area and the SCLC region for indium-doped Cd(Zn)Te crystals, we defined the donor nature of the deep level responsible for the dark conductivity. It is shown that the degree of compensation of the deep level, which is responsible for the dark conductivity, is greater when the level is farther from the middle of the band-gap. We established the relationship between the degree of compensation by the deep level in semiconductor crystals and the detection properties of different structures fabricated on them.

At similar values of the material resistivity, the structures fabricated on the crystals in which dark conductivity is caused by a poorly compensated deep level possess better detection properties.

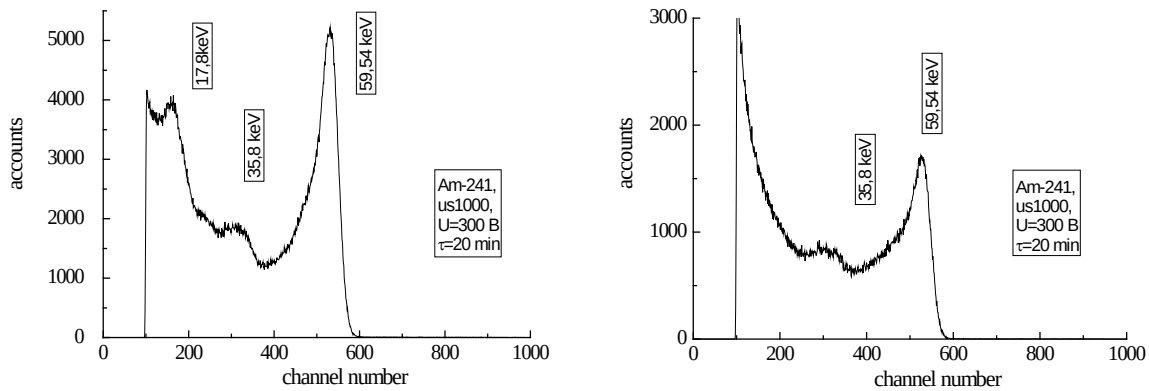

Fig. 10. The energy spectra for an americium-241 isotope measured by the detector fabricated from a crystal of type 1 - *upper* and from a crystal of type 2 – *below*. The voltage was 300 V, and the temperature was 300 K.

Task #2: Processing of customized crystals and device fabrication.

- Data documentation and organization.
- Data analysis.
- Report generation.

<u>Selective Etching Reveals the Migration and Evolution of Dislocations in Annealed $Cd_{1-x}Zn_xTe$</u>

During the solidification of the melt, an ideal crystal free of structural defects should be created. However, as-grown crystals usually show a high density of dislocations and tellurium-rich precipitates and inclusions. One reason for the formation of dislocations is that the crystals are usually grown in quartz ampoules that create additional stress in the solidified material. This stress is relaxed by the formation of linear discontinuities in the crystal's lattice, namely, structural dislocations. In the last few years, much attention has been devoted to the possibility of reducing or removing these extended defects by further thermal treatment of CdTe and CZT wafers. Thermo-migration of Te inclusions in CZT during post-growth

annealing was studied and discussed recently. It was demonstrated that Te inclusions can migrate towards the high-temperature region of the wafer, and leave some smaller particles behind. Moreover, the details of this thermo-migration depend on the specific locations of the Te inclusions within the CZT matrix. We concluded that grain boundaries have a strong trapping effect on the movement of Te inclusions, probably through the high-density zone of dislocation networks in the grain-boundary region. However, the mechanism of migration of dislocations and inclusions and the interrelation between them during annealing remains unclear, despite its importance to the uniformity of charge transport in detectors fabricated from the crystals.

Post-growth annealing, combined with a careful characterization of defects in CZT, helps to clarify the correlation between the post-growth annealing conditions and the mechanism of thermo-migration of the inclusions and the dislocations that surround them. Here, the aim is to improve the material's characteristics and the devices' performance.

The dislocations and other defects in CZT can be successfully revealed by chemical etching of the surface. The most informative selective etchants for CdTe and CZT are a silver-based etchant and a diluted Sirtl with or without light (DSL). Several different kinds of triangular etch pits are revealed by the Inoue etchant, both on the (110) and (111) CdTe surfaces. Other reports show that the Everson etchant can reveal more information about CZT other than just the density of etch pits. Six types of triangular pyramid-shaped etch pits originating from threading dislocations were revealed on the (111)B faces of CZT by the Everson etchant. The DSL etching method proved to be powerful in revealing defects on both the (111)B and (211)B surfaces of CZT single crystals. Nevertheless, the evaluation of these etch pits has not been comprehensive. To meet the demand of obtaining CZT material with a low density of dislocations, the method selected for evaluating dislocations needs to be improved, and the interrelationships between the various dislocations and the growth or post-growth-annealing parameters should be better understood.

The findings mentioned above show that the mechanisms for the formation of dislocations in CZT are very complicated. Such complexity likely comes from the many factors that influence the growth of CZT materials, such as impurities in the melt, the nature of crucible wall, stoichiometry, vibration, and thermal strains. To reveal the origin of the dislocations and eliminate them by improving the growth processes, it is necessary to develop a new evaluation method, and to determine the relationships between various dislocations and inclusions and their technological parameters.

Herein, we detail our systematic research of dislocations in CdTe and CZT and their connection with the migration of inclusions; the approach we adopted was selective chemical etching. We report and discuss our investigation of the influence of annealing on the dislocation behavior in single crystals of CZT and CdTe, and provide results for samples that experienced some degree of Te-inclusion migration following annealing.

To obtain a comprehensive understanding of the physical effects of these processes, we used crystals with various properties (both doped and undoped CdTe), as well as $Cd_{1-x}Zn_xTe$, high and low resistivity crystals, and crystals having different types of inclusions. The total density of dislocations in the crystals evaluated by DSL was estimated to be about 10^4-10^5 cm^{-3}.

The samples used in our experiments were grown by the Vertical Bridgman method (VBM) and by the Traveling Heat Method (THM) (Table 1). The surfaces of the samples were polished sequentially by suspensions of aluminum-oxide powder with a grain size of 1 μm, 0.1 μm, and 0.05 μm. Afterwards, we used a polishing solution of saturated iodine in methanol to remove up to 100 μm of the damaged surface. For several steps of post-growth annealing experiments, we put CdTe or CZT crystals together with the

source of the annealing atmosphere (Cd or Te) into the quartz ampoules and sealed them under a vacuum of 10^{-5} Torr. Samples were annealed in a two-zone furnace with a predetermined temperature profile. Table 1 lists the annealing parameters and properties of the crystals.

For more additional information on the dislocation-mechanism formation, mechanical dislocation rosettes were produced at room temperature on the crystal surfaces (before as well as after each step of the annealing) using a diamond pyramid with the weight of 10 g. The effects of thermal treatment on the defect structure of CdTe and CZT were studied by selective etching. The Bissoli DSL-based CrO_3 and Inoue E1, E2 etchants were used as complementary ones and as the most effective for (111) and (110) oriented crystals, correspondingly. Changes in the quantity and morphology of the inclusions before and after annealing were evaluated by IR transmission microscopy (IRM), optical microscopy, and atomic force microscopy (AFM).

To reveal the influence of two-step annealing processes (first in Cd and next in Te_2 atmosphere) on CZT crystals' mechanical properties and dislocation types, an indentation method was used. Fig. 11 illustrates the damage from inserting the stylus (insert) and the indenter imprint size left on the CZT crystal surface before DSL etching, demonstrating that the crystal hardness diminishes as a result of the annealing. After the indentation of the CZT (111) surface, dislocation loops were formed that were revealed by the Bissoli etchant as star-like "rosettes" from α- and β-dislocations with various degrees of mobility before and after the annealing (Figs. 11a-b). As one can see the identical induced tension caused three times longer rosette's rays after the two-step post-growth annealing. In addition, the "mechanical" dislocations formed slip lines after the annealing.

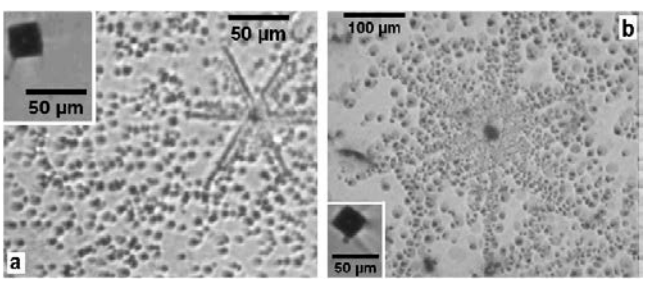

Fig. 11. The CZT-4 surface microphotographs after DSL selective etching of indentation-induced defects before (a) and after (b) post-growth cycling annealing at 873 K, 4 h under maximal cadmium and next under tellurium overpressure.

TABLE 1. Summary of the samples, their properties, and their post-growth annealing parameters.

Sample number	Growth technique, component, electric parameters before the annealing	Inclusion type and Ø before the annealing	Post-growth annealing parameters: step; atmosphere; temperature; time
1. CdTe-1	BM, stoichiometric, p-type, $\sigma = 10^{-2}\ \Omega^{-1}cm^{-1}$	Star-like (10-30 µm), local spherical (5-10 µm)	I cycle: 1st st; P(Cd, max); 973 K; 24 h 2nd st; P(Te_2, max); 1073 K; 4 h II cycle: 1st st; P(Cd, max); 1073 K; 18 h 2nd st; P(Cd, max); 1073 K; 48 h
2. CdTe-2	THM	Small spherical (< 5 µm), local large hexahedral (≤ 50 µm)	1st st. P(Cd max); 1073 K; 4 h 2nd st; P(Te_2 max); 1073 K; 4 h

3. CdTe-3 4. CZT-4	BM BM, Zn	Spherical (≤ 5μm)	I cycle: 1st st; P(Cd,max); 873 K; 4 h 2nd st; P(Te_2 max); 873 K; 4 h II cycle: 1st st; P(Cd max); 973 K; 24 h 2nd st; P(Te_2 max); 1073 K; 4 h
5. CZT-5	BM, Zn, x=0.05 p-type, $\sigma = 5*10^{-4}\ \Omega^{-1}cm^{-1}$	Small inclusions	1st st; P(Cd max); 1123 K, 1 h 2nd st; P(Cd max); 763 K, 50 h
6. CTZ-6	BM, Zn x=0.05		1st st; P(Cd max); 1073 K, 4 h 2nd st; P(Te_2 max); 1073 K, 4 h

Annealing of CZT samples that are nearly transparent by infrared transmission (almost free of Te inclusions) (see Fig. 12a) at P_{Cd}, 873 K for 4 hours resulted in the appearance of stacking faults (Fig. 12b) randomly situated along the surface. Such stacks are visibly inclined to each other at 60° on the (111) faces, and are a characteristic of stacking faults or micro-twins. The last of them disappeared after the next stage of annealing at P_{Te2}, 873 K, 4 h (Fig. 12c). Apart from that, the density of dislocations generally is reduced. We note that the conditions of the post-growth annealing experiments in a Te_2 atmosphere are more limited. It has to be performed at a temperature that is not much higher than the melting point of Te (~700 K), and the duration should not be more than 4 hours. Long annealing times (longer than ~ 4 h) at 1073 K can cause the formation of local Te layers, and even caverns with specific corrosive decorations of the crystal's surface followed by deep Te diffusion into the crystal's volume (Fig. 12d). Undoubtedly, the CZT-Te eutectic forms in some stressed places under such conditions.

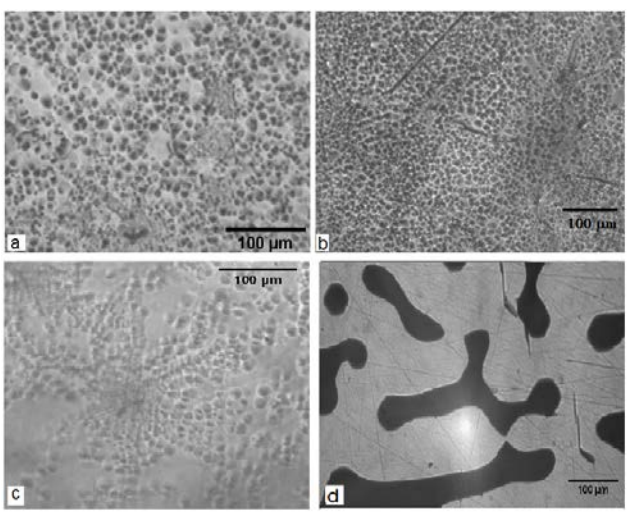

Fig. 12. Microphotographs of the DSL-etched (111) CZT-4 surface: a - before the annealing, b - after post-growth annealing at 873 K for 4 h in Cd vapor; c – after the next step of annealing at 873 K for 4 h under Te_2 vapor; d – deep penetration of tellurium into CZT (black area) after the second step of post-growth annealing at 1073 K under Te_2 vapor for 4 h.

Another situation is observed after the two-step annealing of the CdTe crystals enriched by Te inclusions (see Fig. 13). Based on the data obtained, we concluded that the post-growth annealing under P_{Cd} effectively eliminates only the small (Ø≤10 μm) Te inclusions in the crystals. We observed that the DSL-selective etch pits are relatively dense in places where no Te-based inclusions were visible by IR

transmission. So, inclusions larger than Ø10 μm "disappear" in the IR transmission after short-time (2-4 h) annealing at both over-pressures of P_{Cd} and P_{Te2}. However, their previous positions in pre-annealed samples can be revealed by stress fields in 6-ray rosettes (Fig. 13b) that are similar to ones shown in Fig. 11b.

Herein, we confirm that the factors most limiting for the dissolution of Te inclusions are both the annealing temperature and its duration, especially in the case of annealing at high Te_2 pressure. So, 24-hour annealing in Cd vapor at 973 K resulted in the creation of stacking faults and, probably, a change of the sample's electrical conductivity type, because the Bissoli etchant did not reveal any dislocation-related etch pits (Fig. 13c). Thus, it can be concluded that the stacking faults in CdTe were formed at the higher annealing temperature and longer duration, as compared to CZT.

A high annealing temperature (at 1073 K for 4 h) under Te_2 vapor led to thermal etching of the CdTe sample's surface (Fig. 13d); see Fig. 12d for a comparison with CZT crystals annealed under similar conditions.

The most interesting results were obtained in the case of the annealing of CdTe samples with 'star-like' defects associated with clusters of dislocations punched in the (110) directions. We revealed these defects (size of 20-50 μm) by IR microscopy (Fig. 14a) in crystal CdTe-1 grown by the BM from the melt.

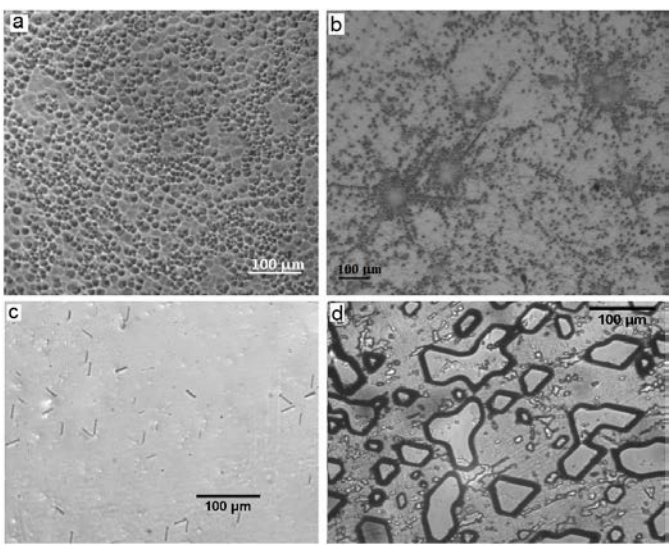

Fig. 13. Optical micrographs of the (111) CdTe-3 surface after DSL etching: a – after 1st 4-hour annealing in Cd vapor at 873 K; b – after 2nd 4-hour annealing in Te_2 vapor at 873 K; c – after 3rd 24-hour annealing in Cd vapor at 973 K (stacking faults formed); and d – thermal etch pits after post-growth annealing at 1073 K for 4 h under Te_2 vapor.

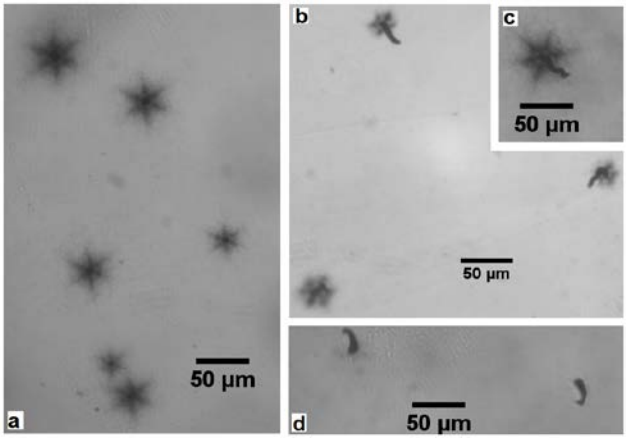

Fig. 14. IR images of inclusions localized in the center of star-like dislocation loops for CdTe-1: a – before the annealing in <111> direction; b – after 1st step of annealing under $P_{Cd,max}$ at 1073 K for 18 h in <110> direction; c – after another 1st step of annealing under $P_{Cd,max}$ at 973 K for 24 h in <111> direction; and d – after 2nd step of annealing under $P_{Cd,max}$ at 1073 K for 48 h in the <111> direction.

Though Cd-rich inclusions were not obtained, the star-like patterns were observed in the crystal's periphery (probably close to the mechanical stress induced near the quartz ampoule walls).

Several BNL papers have described such star-like defects as the center of growth of dislocation loops that are formed at the location of Te inclusions during annealing. However, after annealing we revealed the formation of "tracks" near the center of the star-like inclusions, as reported here for the first time. As evident in Figs. 14b-c, the first step of annealing at 973 K during 24 hours in Cd atmosphere causes a wave-like track near the center of the star-like inclusions. However, after the second step of annealing at higher temperature (1073 K) during 48 hours in a Cd atmosphere, we observe only specific tracks with the central point, but without any visible star-like defects surrounding the inclusions (Fig. 14d). Undoubtedly, tellurium diffused into the crystal from the center of the "rosettes" along one of the "rays" of the dislocation loops, and the local stress was diminished. Pictures *b* and *c* illustrate the results of the same annealed sample in two different projections, namely in the <110> and <111> directions, respectively. Both of these IR images lead to a conclusion about the random way Te appears to diffuse from the center of the defect into the crystal.

We also made an attempt to reveal these specific structural defects on the CdTe (111) surface before the annealing by DSL-selective etching (Fig. 15a) and by investigating their morphology by AFM (Fig. 15d).

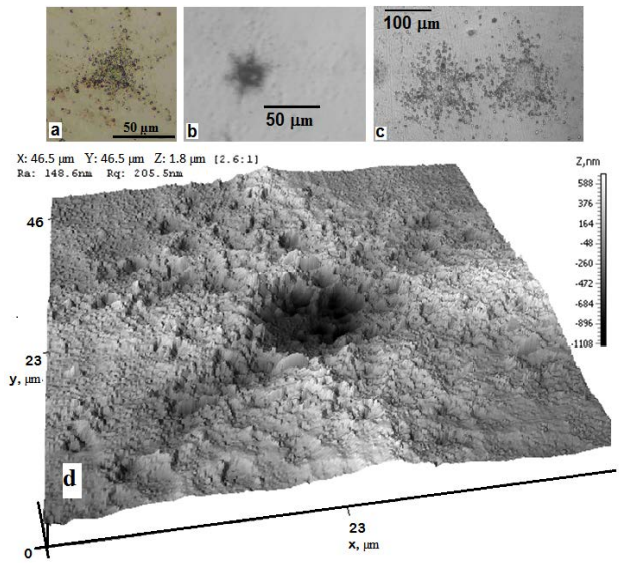

Fig. 15. Microscopic investigations of CdTe-1 crystals surface (scale bar 50 µm); a – star-shaped image of DSL etch pit on the (111) surface before annealing; b – corresponding etch pit after 1st step of annealing under $P_{Cd,max}$ at 1073 K for 18 h; c – similar star-shaped etch-pit formation on the (111) surface for CZT-5 after DSL etching; d – etch-pit morphology investigation by AFM for sample CdTe-1 before annealing.

The depth of the etch pits was less than 1 µm in the center and about 500 nm along the rays of the star. We performed EDX analyses in these specific locations (in center of the star, along the rays, and in the surrounding area) to identify the inclusions in various places of the star-like defect complex (Table 2).

TABLE 2. Elemental EDX analysis of star-like inclusions on the CdTe-1 (111) surface.

Element	Center of star		Ray of the star		Surrounding near the star	
	Mass %	At %	Mass %	At %	Mass %	At %
Se	0.70	0.81	-	-	-	-
Cd	46.09	48.57	45.79	48.64	46.16	48.88
Te	52.44	48.81	53.59	49.91	53.20	49.60
K	0.78	1.81	0.63	1.45	0.64	1.52

In fact, a small amount of selenium was found inside the star-like dislocation loops. This element was not found in either the rays or in the surrounding area of the dislocation loop. Besides that, the defect contained a small quantity of a foreign impurity, potassium. It is widely accepted that various residual impurities can segregate in the liquid tellurium inclusions in as-grown crystals.

Te inclusions can be in the form of small drops that deform the crystal, punching the star-like dislocation loops. This is consistent with studies of Bissoli, who used DSL-chemical etching and SEM to reveal the morphology of Te inclusions in CdTe samples. Unfortunately, we cannot precisely determine the elemental composition of the solid phase at the locations of the tracks that were formed after annealing. It is very difficult to identify this place on the crystal's surface without any additional chemical treatment which, in turn, can influence the results obtained.

In summary, the defect structure of CZT single crystals of different compositions was studied by selective etching. The Bissoli etchant, based on CrO_3, was the most effective for revealing both as-grown and mechanical dislocations on the (111) surface. This etching procedure gives information about the localization

of the dislocation loops, appearing as star-like figures surrounding etch pits. The relationship between the movement of inclusions and the presence of dislocations was investigated by chemical selective etching and optical and infrared microscopy (IRM). We explored the morphology of star-like etch pits with an atomic force microscope (AFM).

We discovered that dislocations act as additional places of stress in crystals for trapping of native atoms or for the localization of inclusions. It was confirmed that native defects and the migration of dopants are affected by dislocations. Small inclusions (less than 10 µm), which are localized near the dislocation, can slowly dissolve during the post-growth thermal treatment at high-temperature equilibrium conditions (900-1000 K). However, excess atoms diffusing from the vapor phase localize on the dislocation loops.

The formation of inclusion tracks in CdTe samples during high-temperature post-growth annealing (970 – 1070 K) were revealed near the center of the star-shaped dislocation loops by infrared transmission. The track formation confirms the strong trapping effect of dislocation migration associated with the inclusions in CdTe crystals. Such detailed investigations in conjunction with other experimental methods, for example EDX analysis near the dislocation loops, can give valuable local information about the nature of inclusions, their stoichiometric composition, and a deeper understanding of the mechanism of migration of inclusions in materials, which is needed for better control and improvement of their electro-physical characteristics.

The local elemental composition of material in the center of the dislocation loops, along the rays, and near the local star- shaped dislocation was determined by EDX. Small amounts of selenium and potassium were revealed only in the center of the star-like inclusions after the chemical treatment.

Bissoli's etchant offers the possibility of identifying the (111) surface and revealing the grain boundaries and twins. Comprehensive characterization of etch-pit localization after both Inoue (E-Ag2) and Bissoli etchants is complementary, and they are the most effective solutions for revealing dislocations in CdTe crystals by selective etching.

Our investigation opens new opportunities for the realization of selective-etching methods for revealing dislocations and better characterization of crystal quality. The selective etching method is an easy, visual and unique one for revealing dislocations on the CdTe and CZT surface, which gives us the capability to obtain information about the localization of the defects and complements EDX and other experimental investigations.

Task #3: Simulate the effects of dislocations and sub-grain boundaries on CZT device performance and establish bounds on the degree to which they can be tolerated for thick (> 10 mm) detectors. Model the defects in and around twins and sub-grain boundaries and simulate their effects on carrier transport.

No additional comments for this quarter.

COSTING: We update the webPMIS cost fields monthly. All spending is in accordance with schedule.

TECHNICAL REPORTS/PUBLICATIONS:

PEER REVIEWED PUBLICATIONS:

1. V. Sklyarchuk, P. Fochuk, Z. Zakharuk, I. Rarenko, Ye. Nykoniuk, O. F. Sklyarchuk, A. E. Bolotnikov, and R. B. James, "The Impact of Compensation on the Detection Properties of n-Cd(Zn)Te Crystals", IEEE Trans. on Nuclear Science, submitted December 2015.

2. O. Korovyanko, I. Nakonechnyi, L. Shcherbak, P. Fochuk, A. E. Bolotnikov, G. Yang and R. B. James, "Selective Etching Reveals the Migration and Evolution of Dislocations in Annealed $Cd_{1-x}Zn_xTe$", IEEE Trans. on Nuclear Science, submitted December 2015.

3. Wonho Lee, Aleksey Bolotnikov, Taewoong Lee, Giuseppe Camarda, Yonggang Cui, Rubi Gul, Anwar Hossain, Roy Utpal, Ge Yang, and Ralph James, "Mini Compton Camera Based on an Array of Virtual Frisch-Grid CdZnTe Detectors", IEEE Trans. on Nuclear Science, submitted December 2015.

4. P. Fochuk, Ye. Nykoniuk, Z. Zakharuk, O. Kopach, N. Kovalenko, A. E. Bolotnikov, and R. B. James, "Micro-heterogeneity in Semi-insulating Cd(Zn)Te Crystals", IEEE Trans. on Nuclear Science, submitted December 2015.

5. U. N. Roy, R. M. Mundle, G. S. Camarda, Y. Cui, R. Gul, A. Hossain, G. Yang, A. K. Pradhan, and R. B. James, "Novel ZnO:Al contacts to CdZnTe X- and gamma-ray detectors", Journal of Appl. Phys., Submitted December 2015.

OTHER PUBLICATIONS:

None.

PRESENTATIONS:

1. A. E. Bolotnikov, G. S. Camarda, E. Chen, Y. Cui, G. De Geronimo, C. Finfrock, J. Fried, A. Hossain, G. Mahler, M. Petryk, U. Roy, S. Taherion, E. Vernon, G. Yang, R. B. James, "Feasibility of CdZnTe Gamma–Ray Detectors with Thicknesses >15 mm", R1B-6, Invited Presentation, IEEE International Symposium on Room–Temperature Semicondctor Detectors, November 2, 2015, San Diego, CA.

2. U. N. Roy, A. E. Bolotnikov, G. S. Camarda, Y. Cui, R. Gul, A. Hossain, R. Tappero, G. Yang, R. B. James, "Role of Selenium in CdTe–Based Host Materials for Radiation Detector Applications", R1D-3, IEEE International Symposium on Room–Temperature Semiconductor Detectors, November 2, 2015, San Diego, CA.

3. U. N. Roy, A. E. Bolotnikov, G. S. Camarda, Y. Cui, R. Gul, A. Hossain, G. Yang, R. B. James, A. K. Pradhan, R. M. Mundle, "Novel Non-Metallic Contact on CdTe-Based Materials", Invited Presentation, R2B-5, International Symposium on Room–Temperature Semiconductor Detectors, November4, 2015, San Diego, CA.

4. A. M. Hossain, A. E. Bolotnikov, G. S. Camarda, Y. Cui, U. N. Roy, G. Yang, R. B. James, "Response Non–Uniformity in Large–Volume Detector–Grade CZT Crystals", R2D-3, IEEE International Symposium on Room–Temperature Semiconductor Detectors, November 3, 2015, San Diego, CA.

5. G. Yang, U. Roy, A. E. Bolotnikov, Y. Cui, G. S. Camarda, A. Hossain, R. Gul, R. B. James, "Optical and Electrical Properties of CdZnTe and CdZnTeSe Crystals for Radiation Detector Applications", R2D-4, IEEE International Symposium on Room–Temperature Semiconductor Detectors, November 3, 2015, San Diego, CA.

6. O. Korovyanko, I. Nakonechnyi, L. Shcherbak, P. Fochuk, A. Bolotnikov, R. B. James, "Revealing of Dislocations Migration in CdZnTe in Conjunction with Inclusions During Post–Growth Annealing by Selective Etching", Poster Presentation, R3A-5, IEEE International Symposium on Room–Temperature Semiconductor Detectors, November 4, 2015, San Diego, CA

7. P. Fochuk, Y. Nykoniuk, Z. Zakharuk, I. Rarenko, N. Kovalenko, A. Bolotnikov, R. B. James, "Micro–heterogeneity in Semi–insulating Cd(Zn)Te", Poster Presentation, R3A-11, IEEE International Symposium on Room–Temperature Semiconductor Detectors, November 4, 2015, San Diego, CA.

8. V. Sklyarchuk, P. Fochuk, Z. Zakharuk, I. Rarenko, Y. Nykoniuk, V. Sandulov, A. Bolotnikov, R. B. James, "The Impact of Compensation on the Detection Properties of n–Cd(Zn)Te Crystals", Poster Presentation, R3A-12, IEEE International Symposium on Room–Temperature Semiconductor Detectors, November 4, 2015, San Diego, CA.

9. R. Gul, S. Egarievwe, A. Bolotnikov, G. Camarda, Y. Cui, A. Hossain, U. Roy, G. Yang, R. B. James, "The Effects of Point Defects on the Electrical Transport Properties and Performance of CZT Radiation Detectors", Poster Presentation, R3A-15, IEEE International Symposium on Room–Temperature Semiconductor Detectors, November 4, 2015, San Diego, CA.

10. Y. Chen, Y. Cui, P. O'Connor, G. S. Camarda, A. Hossain, U. Roy, G. Yang, R. B. James, "Test of a 32–Channel Prototype ASIC for Photon–Counting Applications", Poster Presentation, R3A-35, IEEE International Symposium on Room–Temperature Semiconductor Detectors, November 4, 2015, San Diego, CA.

11. G. S. Camarda, A. Bolotnikov, Y. Cui, R. Gul, A. Hossain, U. Roy, G. Yang, R. B. James, "Characterization of Semiconductor and Scintillator Detectors at the Advanced Light Source (ALS)", R3C-5, IEEE International Symposium on Room–Temperature Semiconductor Detectors, November 4, 2015, San Diego, CA.

12. K. H. Kim, P. Kim, C. Park, S. Cho, J. Lee, G. Camarda, A. Hossain, A. Bolotnikov, R. B. James, "Spectroscopic Properties of CdMnTe Detector Grown by Seedless THM", Invited Presentation, R5B-2, IEEE International Symposium on Room–Temperature Semiconductor Detectors, November 6, 2015, San Diego, CA.